Case Studies in Thermal Engineering 33 (2022) 101932

Contents lists available at ScienceDirect

Case Studies in Thermal Engineering

journal homepage: www.elsevier.com/locate/csite

Experimental and simulation investigation of 3-D soot temperature and volume fraction fields of afterburner flame

Minglu Dai [a], Bin Zhou [a,*], Jianyong Zhang [b], Bingxian Zuo [a], Yihong Wang [a]

[a] School of Energy and Environment, Southeast University, Nanjing, 210096, China
[b] School of Computing, Engineering and Digital Technologies, Teesside University, TS1 3BA, UK

GRAPHICAL ABSTRACT

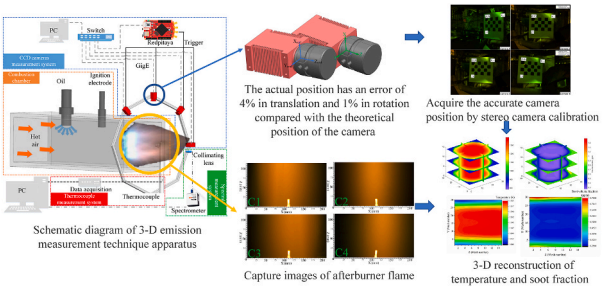

ARTICLE INFO

Keywords:
Afterburner flame
CCD camera
Soot temperature
Soot volume fraction
Stereo camera calibration

ABSTRACT

The temperature and soot volume fraction in afterburn flame are very important parameters in flame analysis and burner design. A novel method that combines the 3-D emission measurement technique and the camera position and attitude calibration by using the translation and rotation matrix is proposed. The spectral intensities of oxygen-enriched combustion and afterburner flame facility were designed for testing purposes. The theoretical analysis and experimental results are provided in this paper. The results demonstrated that this novel technique can provide good measurement accuracy with high spatial resolution.

1. Introduction

The afterburner of an aircraft engine is vital because it can provide huge thrust in a short time. However, the violent combustion reaction in the afterburner can also lead to overheating, noise, vibration, and equipment deterioration [1,2]. Hence, the diagnosis of

* Corresponding author.
E-mail address: zhoubinde@seu.edu.cn (B. Zhou).

https://doi.org/10.1016/j.csite.2022.101932
Received 18 January 2022; Received in revised form 5 March 2022; Accepted 9 March 2022
Available online 14 March 2022

combustion flame temperature and composition concentration is of great significance in the investigation of the reaction process and optimization of the structural design for an afterburner.

The spectrally resolved measurement method has been widely used to obtain the flame temperature and soot concentration. Bheemul et al. [3] employed three CCD cameras placed uniformly around an axisymmetric gaseous flame, the result showed that the 3-D flame structure could be reconstructed by using this method. Then, many researchers adopted this technology in thermal engineering. Lou et al. [4] investigated the 2-D flame temperature distribution in a pulverized coal-fired furnace based on the flame radiation method. Zhou et al. [5] used eight CCD cameras to measure the flame radiation in a pulverized-coal-fired furnace, and the relationship between the flame radiation and 3-D temperature distributions was established in a large-scale pulverized-coal-fired boiler furnace. Chu et al. [6] reconstructed the flame image of a controlled circulation boiler by multiple image detectors, with which, the distributed parameter model for the evaporation system was verified.

With the application of spectrally resolved measurement methods in thermal engineering, lots of researchers focused on improving the measurement accuracy. Liu et al. [7] concluded that the number of cameras ought to be greater than 4 and the signal-to-noise ratio needs to be better than 54 dB to obtain the 3-D soot volume fraction field even for a small asymmetric flame. Yan et al. [8] focused their study on the soot emission intensities within a visible and infrared wavelength range to establish a relationship between soot concentration and flame temperature, which provided a way for simultaneous reconstruction of 2-D distributions of temperature and soot volume fraction. This method has also been used in flame measurement for municipal solid waste combustion [9]. Then, he focused on the effect of self-absorption during the combustion process, the result proved that this method is reliable and can be used for combustion diagnosis [10]. Zhang et al. [11] acquired three different image formats to probe the flame temperature in a 5000 t/h cement rotary kiln, and the results indicated that the error of raw image processing was below 2% in 500–3000 K, similar to that a typical infrared pyrometers can achieve over the same range. Many researchers have also enhanced the spectrally resolved information with the aid of liquid crystal tunable filters (LCTF), which called multispectral imaging technology [12]. For instance, Ni et al. [13] installed LCTF between camera and lens to study the laminar flame. Their results indicated that the average error of the multi-wavelength method for the reconstructed volume fraction has improved to 3.17%. Li et al. [14] pointed out that the multi-wavelength method has the advantages of four times higher accuracy than the two-color method. Although the LCTF could increase the spectrally resolved information, the spectral information of different bands cannot be collected at the same time, which is lead to a reduction in time resolution and is a drawback of this method.

It can be seen from Table 1 that the high spatial resolution is one of the advantages of the spectrally resolved measurement method. However, the research results were unsatisfactory in terms of measurement accuracy. The key challenge for such systems has been that the 3-D system reconstruction accuracy is determined directly by the position and attitude among cameras, which are affected by the external parameter errors [15]. This problem has yet to be addressed in 3-D emission measurement. The stereo calibration method can be used not only to estimate the internal and external parameters for each camera but also to gain the relative position of these cameras [16]. The average calibration errors can be as low as 0.249 mm and 0.027 mm for all cameras in coarse and fine situations respectively as claimed in the literature [17].

The investigation presented in this paper is a 3-D emission measurement technique, which adopts the stereo camera calibration method. Developed by the authors of this paper, this technique uses multiple cameras to guarantee a high spatial resolution, and the camera position and attitude are corrected through the translation and rotation matrix in the stereo camera calibration process to improve the measurement accuracy. The experimental results in an afterburner rig achieved good balances between accuracy and spatial resolution.

2. Experimental and reconstruction methods

2.1. Experimental methodology

Fig. 1 illustrates the experimental setup, which was composed of a combustion chamber, CCD cameras, spectrum, and thermocouple measurement systems. The combustion chamber was constructed with a square stainless-steel sheet. The inside size of the chamber was 200 mm × 200 mm. High-temperature air was supplied at the inlet of the burner. Eight nozzles mounted on a pipe around the burner were used to inject aviation kerosene (RP-3) into the combustion chamber. An electric spark-generating electrode was utilized to ignite the RP-3/air mixture. It should be noted that the input air and aviation kerosene were precisely controlled to maintain stable flames throughout the experiments.

Table .2 shows the feature and specifications of measurement devices. Four CCD cameras were evenly spaced around one side of the burner, which constituted the CCD camera measurement system in the experiments. The distance between the center of the square outlet and each of the four CCD sensors was equal, and the angle between any two adjacent cameras was 45°. A Red Pitaya was used to generate a pulse-width modulation (PWM) signal to trigger four CCD cameras synchronously. These cameras were powered, and data were transmitted with the switches via power over ethernet (PoE). A fiber with a collimator was mounted on one of four cameras,

Table 1
The comparison of different measurement techniques.

	Costs	Spatial resolution	Temporal resolution	Accuracy	Contact or Non-contact measurement
This research technology	Middle	High	High	Low	Non-contact measurement
Multispectral imaging technology [13,14]	High	Middle	Low	High	Non-contact measurement
Thermocouple [5]	Low	Low	Middle	Middle	Contact measurement

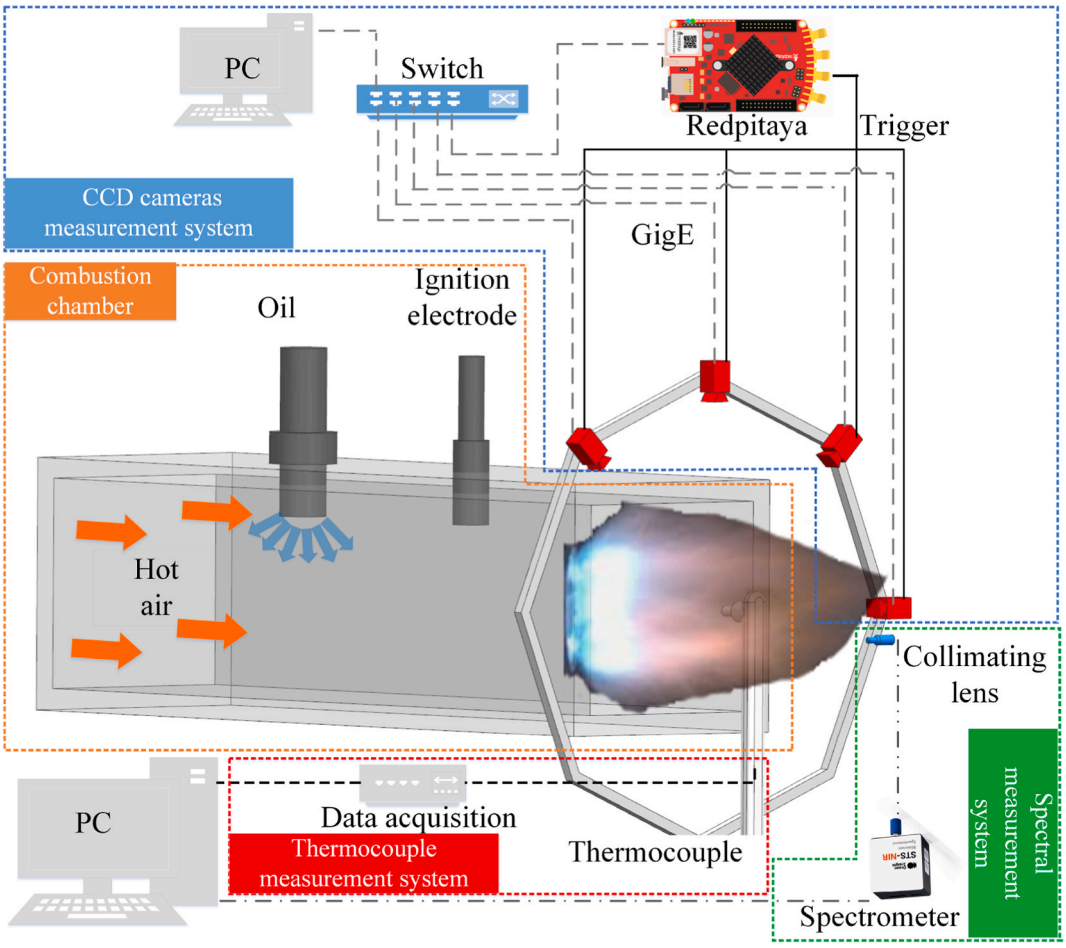

Fig. 1. Schematic diagram of the experimental apparatus.

Table 2
The feature and specifications of measurement devices.

Device	Feature	Specification	Feature	Specification
CCD cameras	Sensor model	Sony ICX445AQA	Resolution	1280 (H) × 960 (V); 1.2 MP
	Shutter type	Global shutter	Sensor type	Interline CCD, Progressive Scan
	Sensor format	Type 1/3	Pixel size	3.75 μm × 3.75 μm
	Max. frame rate at full resolution	33.3 fps	RGB color pixel formats	RGB8Packed, BGR8Packed
	Default lens mount	C-Mount	Exposure time control	12 μs to 77.3 s; 1 μs increments
	Power consumption	External power: 2.9 W at 12 VDC Power over Ethernet: 3.5 W	Trigger latency	2 μs
B type thermocouple	measuring range	500–1800 °C	Accuracy	±0.25% of range
	Temporal resolution	2 Hz	Diameter	1 mm
Spectrograph	Model	STS-VIS	Sensor model	ELIS1024
	Spectral range	350–800 nm	Integral time	10 μs - 10 s
	Signal to Noise Ratio (SNR)	>1500:1	Dark noise	≤3 counts rms
	Raster	600 g/mm	Slit	10, 25, 50, 100 or200 μm

which was connected to the spectrograph. The fiber, collimator, and spectrograph were comprised of a spectral measurement system, which was connected to the laptop via a USB cable for simultaneous spectral signal transmission and power provision. The thermocouple measurement system contained a B-type thermocouple, a pair of thermocouple extension cords, and an acquisition device. The thermocouple was protected by a circular alundum tube, which was placed at the center of the square outlet behind the CCD cameras. The electrodynamic force caused by temperature change was collected by the acquisition device and converted to degrees Kelvin. Thermocouples need velocity and radiation correction before experimental because they work in high temperature and jet stream environments.

To acquire the precise position of each camera relative to the flame, the following steps were adopted. Firstly, the camera position was adjusted manually. The six-degree-of-freedom displacement machine was mounted on regular octagonal support with an inscribed circle diameter of 560 mm so that the distance between each CCD detector and the central axis of flame was equal. Then, cameras were adjusted through the six-degree-of-freedom displacement machine to ensure that the thermocouple appeared in the same row and column in the captured image. This means that the thermocouple was served as a reference for the four cameras because the thermocouple was in the center of the flame. Secondary, the stereo camera calibration method [18,19] was used to calculate the precise position of cameras. The calibration specimen was made of aluminum with a dimension of 100 mm × 100 mm. There were 12 black squares with each side dimension of 20 mm on the calibration specimen, and the manufacturing tolerance of each square was ± 0.005 mm. The calibration processes were conducted three times because only two cameras could be calibrated each time. The requirement for the overall mean error of calibration in pixels was better than 0.2 pixels to ensure the calibration accuracy.

The world coordinate system was established with the direction of the flame jet as the positive direction of the *Z*-axis, the direction pointing to the camera CCD from the center as the positive direction of the *X*-axis, and the center of reconstruction area as the origin. Table .3 provides the translation and rotation matrix of four cameras, where α, β, and θ are rotation angles with *X*, *Y*, and *Z* as the rotation axes respectively, and the positive sign indicates clockwise rotation about the axis. Comparing the theoretical to the measured results, it is clear that manual adjustment of the camera could not meet the position accuracy requirement. The camera position error was controlled in the region of 5 mm–10 mm, and the camera angle error was in 0.2°–5° in the experiments.

2.2. Reconstruction method

Fig. 2 illustrates the reconstruction method of this experiment, where the size of the reconstruction space $L \times W \times H$ is 200 mm × 200 mm × 100 mm. The dimension of *L* and *W* is the same as that of combustion chamber outlet. The direction of *H* is with the flame. The reconstructed area was discretized to $N_X \times N_Y \times N_Z$ volume elements, and the sequence of these volume elements could be found in this figure. It was revealed that the relative position among these cameras has a great influence on the accuracy of path calculation L_{path}, so it's very important to acquire the precise relative position among these cameras.

According to the stereo camera calibration method, the path L_{path} ought to be corrected, and the true beginning and ending points of path L_{path} can be corrected as:

$$\begin{bmatrix} X_c \\ Y_c \\ Z_c \end{bmatrix} = R_c \cdot \begin{bmatrix} X_0 \\ Y_0 \\ Z_0 \end{bmatrix} + \begin{bmatrix} T_x \\ T_y \\ T_z \end{bmatrix} \tag{1}$$

where the X_C, Y_C, Z_C are referred as the corrected positions, X_0, Y_0, Z_0 are theoretical positions, T_x, T_y, T_z are the translation matrix, and R_c is the rotation matrix, which can be expressed as:

$$\begin{bmatrix} \cos(\beta)\cos(\theta) & \cos(\beta)\sin(\theta) & -\sin(\beta) \\ -\cos(\alpha)\sin(\theta)+\sin(\alpha)\sin(\beta)\cos(\theta) & \cos(\alpha)\cos(\theta)+\sin(\alpha)\sin(\beta)\sin(\theta) & \sin(\alpha)\cos(\beta) \\ \sin(\alpha)\sin(\theta)+\cos(\alpha)\sin(\beta)\cos(\theta) & -\sin(\alpha)\cos(\theta)+\cos(\alpha)\sin(\beta)\sin(\theta) & \cos(\alpha)\cos(\beta) \end{bmatrix} \tag{2}$$

The parameters α, β, and θ are rotation angles to *X*, *Y*, *Z* coordinates, T_x, T_y, T_z are translation matrix, and all of those parameters can be obtained through stereo camera calibration.

In this study, the reconstruction theory is based on the assumption that the effect of scattering, self-absorption, and background incident emission is negligible, which is supported by other scholars in their work including the three-dimensional temperature distributions visualization [18], the spectrally resolved flame emission measurement [21], and the multispectral imaging system [13].

According to the projection law, the detected radiation intensity $I_\lambda(L_{\mathrm{path},m})$ of each CCD in the camera at one of the line-of-sight directions p_s can be written as:

Table 3
The theoretical and measured position of cameras.

			Camera1 to Camera 2	Camera 1 to Camera 3	Camera 1 to Camera 4
Translation (mm)	X	Theoretical	−164.0202	−560	−955.9797
		Measured	−177.2563	−569.6190	−967.4157
	Y	Theoretical	395.9797	560	395.9797
		Measured	382.3205	540.9161	385.7774
	Z	Theoretical	0	0	0
		Measured	−6.4933	2.5984	5.0712
Rotation (degree)	α	Theoretical	0	0	0
		Measured	−1.7085	−0.8788	1.6527
	β	Theoretical	0	0	0
		Measured	0	0	0
	θ	Theoretical	−45	−90	−135
		Measured	−44.1781	−88.4702	−133.112

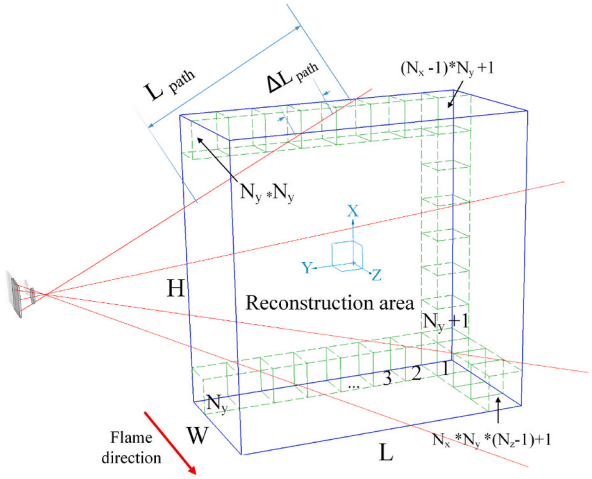

Fig. 2. The schematic of calculating path.L_{path}

$$
\begin{aligned}
I_\lambda\left(L_{path,m}\right) &= \int_0^{p_s}\left[\kappa_\lambda(p)I_{b,\lambda}(p)\right]dp \\
&= \sum_{\mathrm{n}=1}^{N}\kappa_\lambda(\mathrm{n})I_{b,\lambda}(n)l_{L_{path,m}}(n) \\
&= \sum_{n=1}^{N}H_\lambda(n)l_{L_{path,m}}(n)
\end{aligned}
\tag{3}
$$

where the $\kappa_\lambda(p)$ refers to the soot absorption coefficient of the volume element n. The $l_{L_{path,m}}(n)$ is the length of the ray in the volume element n. The $I_{b,\lambda}(n)$ represents the monochromatic blackbody radiative intensity of the volume element n, which can be calculated using the following formula:

$$
I_{b,\lambda}(n) = \mathrm{c}_1 \,/\, \lambda^5 e^{(c_2/\lambda T_n - 1)} \tag{4}
$$

In this expression, c_1 and c_2 are the first and second radiative constants respectively.

The afterburning flame was investigated in this experiment, where the particles in flame had a mode diameter varied between 12 and 28 nm, which was within the Rayleigh range, hence, the soot absorption coefficient was calculated using the following formula according to the work conducted by Modest et al. [20]:

$$
\kappa_\lambda = \frac{36\pi NK}{\left(N^2 - K^2 + 2\right)^2 + 4N^2K^2}\frac{f_v}{\lambda} \tag{5}
$$

This expression can provide the soot absorption coefficient with sufficient accuracy, where N and K can be obtained with the following set of formulae:

$$
\begin{aligned}
N &= 1.811 + 0.1263\ln\lambda + 0.027\ln^2\lambda + 0.0417\ln^3\lambda \\
K &= 0.5821 + 0.1213\ln\lambda + 0.2309\ln^2\lambda - 0.01\ln^3\lambda
\end{aligned}
\tag{6}
$$

To accomplish the 3-D soot temperature and volume fraction reconstruction, the reconstruction area was discretized. Assume that the total number of spatial meshes was N_{all}, and the total number of rays captured by the camera CCD detector was M_{all}, hence, the correction path length matrix can be written as:

$$
I_\lambda(M_{all}) = A_c H_\lambda(N_{all}) \tag{7}
$$

where $I_\lambda(M_{all}) = (I_\lambda(1), I_\lambda(2)\cdots I_\lambda(M_{all}))^T$, $H_\lambda(N_{all}) = (H_\lambda(1), H_\lambda(2)\cdots H_\lambda(N_{all}))$, and A_c is the matrix of the corrected path length for each ray passing through the reconstruction region, which can be obtained from Eq. (1).

To improve the spatial accuracy of the reconstruction area, more rays traversed this area should be employed, so the matrix $H_\lambda(N_{all})$ is a large sparse matrix. The H_λ of each mesh can be obtained by finding the upper and lower bounds through solving the following least-squares problem,

$$
\begin{aligned}
&\text{minimize} \quad \|Ax - b\|_2 \\
&\text{subject to } l \le x \le u
\end{aligned}
\tag{8}
$$

where l and u are the lower and upper boundaries of H_λ. In order to solve this equation, some scholars adopted the 2-D Tikhonov

regularization to discretize the gradient matrix [21,22]. In the 2D Tikhonov regularization, S_{2D} is rank-deficient matrix, $\delta S_{2D} = 0$, and the S_{2D} can be used to smooth the reconstruction results, Eq. (8) can be further improved to:

$$\begin{aligned} &\text{minimize} \quad \left\| \begin{bmatrix} A \\ \delta S_{2D} \end{bmatrix} x - \begin{bmatrix} b_{2D} \\ 0 \end{bmatrix} \right\|_2 \\ &\text{subject to} \quad l \le x \le u \end{aligned} \tag{9}$$

where δ is the regularization parameter that controls the pertinence of the penalty term compared to the residual norm. The focus of the 2-D Tikhonov regularization is on the relationship between unsolved x on the plane, the 3-D Tikhonov regularization in this research is used to establish the relationship between unsolved x and neighboring voxels, which can be written as [23]:

$$\begin{aligned} &\text{minimize} \quad \left\| \begin{bmatrix} A \\ \delta S_{3D} \end{bmatrix} x - \begin{bmatrix} b_{3D} \\ 0 \end{bmatrix} \right\|_2 \\ &\text{subject to} \quad l \le x \le u \end{aligned} \tag{10}$$

where S_{3D} is the discrete 3-D gradient matrix, and its detailed expression is given below:

$$S_{3D,\text{ij}} = \begin{cases} 1 & \text{if } i = j \\ -1/n_i & \text{if element i neighbors element } j \\ 0 & \text{otherwise} \end{cases} \tag{11}$$

In the 3-D Tikhonov regularization, $n_i = 6$, which means each element n has 6 neighbor elements. The CVX tools in MATLAB were used to transform the least-squares problem into a quadratic program to achieve high accuracy and computational efficiency [24].

Once $H_\lambda(n)$ is obtained in each volume element using $H_\lambda(n) = \kappa_\lambda(n) I_{b,\lambda}(n)$, where $\kappa_\lambda(n) I_{b,\lambda}(n)$ can be substituted based on Eq. (4) and Eq. (5), thus,

$$\begin{aligned} &H_\lambda(n) = 6\pi f_v(n) E(m) c_1 / \lambda^6 \pi e^{c_2/\lambda T_n} \\ &\frac{E(m)}{H_\lambda(n)\lambda^6} = \frac{e^{c_2/\lambda T_n}}{6\pi f_v(n) c_1} \\ &\ln\left(\frac{E(m)}{H_\lambda(n)\lambda^6}\right) = \frac{c_2}{T_n}\frac{1}{\lambda} - \ln(6\pi f_v(n) c_1) \end{aligned} \tag{12}$$

In this set of equations, $1/\lambda$ is an independent variable, $\ln\left(\frac{E(m)}{H_\lambda(n)\lambda^6}\right)$ the dependent variable, $\ln(6\pi f_v(n) c_1)$ the intercept; therefore, the last function in Eq. (12) can be regarded as a linear function same as $y = kx + b$. Two kinds of $H_\lambda(n)$ formed under the wavelength of 535 nm and 610 nm can be used to solve this linear function, because the CCD detectors have well spectral response and absolute quantum efficiency under the wavelengths. The temperature T_n in the equation can be found using $T_n = \frac{c_2}{k_n}$. The soot volume fraction can be determined from $f_v(n) = \frac{e^{-b_n}}{6c_1}$.

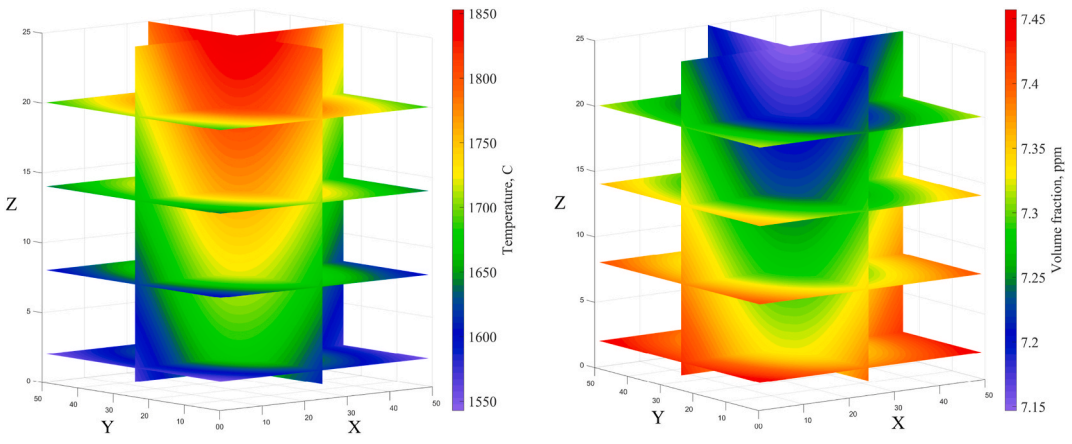

(a) Temperature (b) Soot volume fraction

Fig. 3. 3-D distribution of soot temperature and volume fraction.

3. Results and discussions

3.1. The effect of camera offset

The experiments were conducted on the testing rig shown in Fig. 1. The 3-D distribution of soot temperature and volume fraction over the reconstruction area are displayed in Fig. 3, which verifies the flame structure and 3-D distribution obtained by Gu et al. [25]. The reconstruction area was discretized into four different mesh densities, including 10*10*5, 20*20*10, 30*30*15, and 40*40*20 elements.

The relative error was used to evaluate the accuracy of soot temperature and volume fraction reconstruction, which constituted by the theoretical model, camera position, and reconstruction algorithm, and can be defined as:

$$E_{\mathrm{rel}} = \frac{\left|\alpha_{\mathrm{n}}^{\mathrm{h}} - \alpha_{\mathrm{n}}^{\mathrm{r}}\right|}{\alpha_{\mathrm{n}}^{\mathrm{h}}} \times 100\% \tag{13}$$

where the α_n^h and α_n^r are the hypothesis and reconstruction temperature or soot volume fraction in volume element n, respectively.

The reconstruction results of the sparsest (10*10*5) and the densest (40*40*20) meshes are demonstrated in Fig. 4. The horizontal axis, i.e., the volume element sequence which can be found in Fig. 2. The scatter points in the figure represent the relative reconstruction errors of soot temperature and volume fraction at a given volume element. It can be seen that in each layer of the *X*–*Y* face along the *Z*-axis, the relative errors of either temperature or volume fraction reached the peak at the center of this layer of the mesh. Additionally, the peak relative error of all mesh occurred around the body center of the reconstructed area. For the same mesh density, the relative error of volume fraction was larger than that of temperature. However, when the mesh size was set as 40*40*20, the relative error peak values of temperature and volume fraction appeared at the body center of the reconstruction area, and the relative error was larger than 1%.

The average relative errors for four different mesh densities are dissected in Fig. 5. The results demonstrate that the relative error was greatly reduced after the translation and rotation offset of cameras were corrected for all four different mesh densities. Moreover, the relative measurement errors of temperature and volume fraction were higher with increased mesh density. It can be seen that the

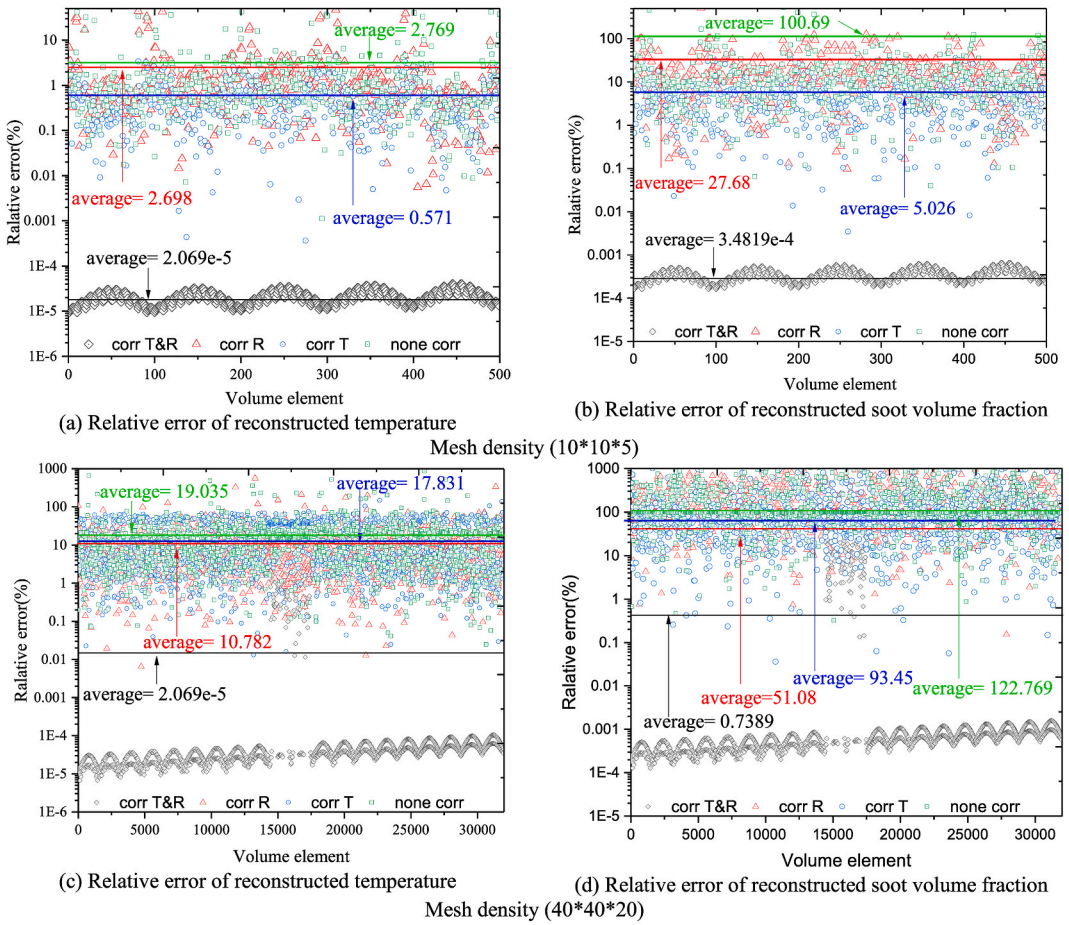

Fig. 4. Relative error of reconstructed soot temperature and volume fraction for different mesh densities.

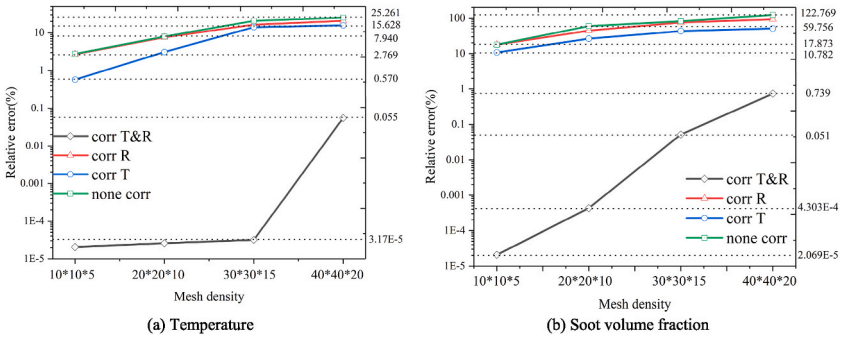

Fig. 5. Average relative error of different mesh density.

relative error of temperature was lower than 3% for the mesh density of 10*10*5, however, without the correction of transfer and rotation offset, the relative error of volume fraction was 10.782%. This reveals how important it is to correct the translation and rotation offsets of cameras for high-precision reconstructions of temperature and volume fraction.

The average relative error with only rotation correction was much higher than that with only translation correction for either temperature or volume fraction reconstruction. In other words, the offset of camera position contributed more than that of camera angle to the reconstruction error. The reason was that the translation offset was larger than rotation offset in this experiment. If neither of these two offsets was calibrated, the reconstruction error could be even larger.

It can be predicted that the relative error of temperature is 0.055% for the mesh density of 40*40*20 if both the translation and rotation offsets are corrected, whereas the average error of soot volume fraction can be as good as 0.739%.

Fig. 6 shows the relative errors when both translation and rotation were corrected for mesh density of 30*30*15. It can be found that the shape constituted by the scattered points over the volume element range of 5401–13500 is clearer than that over the range of 1–5400, i.e., the relative errors within the range of 1–5400 had a good consistency. The relative errors of temperature and soot fraction were less than 0.002%. Hence, the mesh density of 30*30*15 was adopted in this research to maintain the mesh density and numerical accuracy simultaneously.

3.2. *Experimental results and discussion*

The key to the spectrally resolved measurement of flame radiation is avoiding the interference of chemiluminescence. The spectrum of the oxygen-enriched flame shows the typical characteristics of chemiluminescence: a. the flame radiation intensity is very weak; b. There are obvious emission peaks [26]. The intensity of afterburner flame in the testing rig described in Fig. 7 is smooth and increasing with wavelength. Due to the high emissions intensity of soot, chemiluminescence was annihilated, so there is no emissions peak. Hence, the resolved measurement of flame radiation method can be used in this research [27,28].

The stereo camera calibration method and 3-D emission measurement technique were adopted to investigate the soot temperature and volume fraction of afterburner flame in the testing rig described in Fig. 1 to verify the practical validity. In this experiment, the fuel flow rate was set at 21.63 g/s, the air co-flow rate was 0.894 kg/s, and the airflow temperature was controlled at 800.9 K. Fig. 8 shows the images of afterburner flame generated by the experimental apparatus at different times, and in these pictures, the reconstruction area was dispersed into a mesh density of 30*30*15 elements. The pictures captured by the four cameras at different times were used to

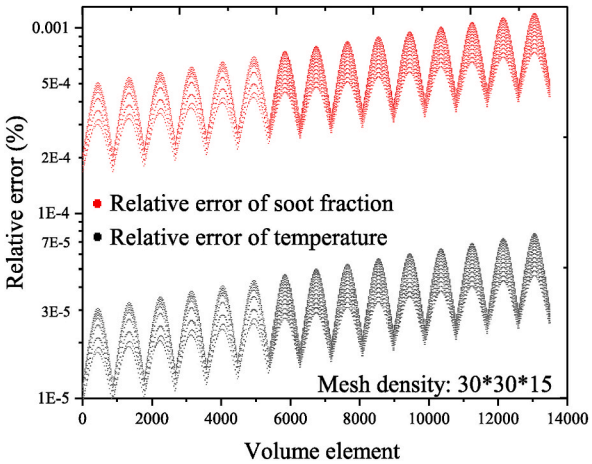

Fig. 6. Relative error of translation and rotation corrected at mesh density of 30*30*15.

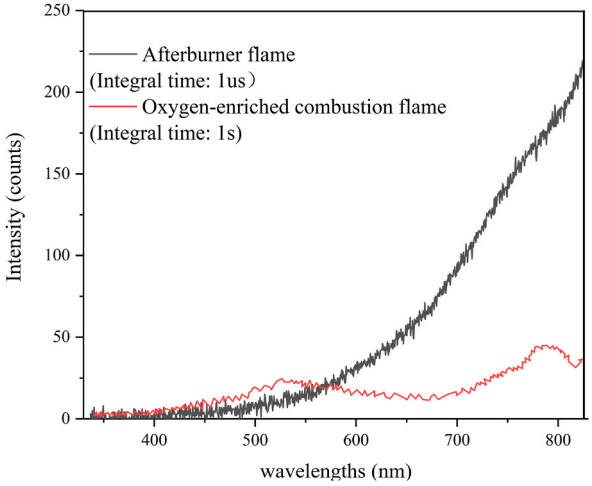

Fig. 7. Spectral intensities of Oxygen-enriched combustion and afterburner flame.

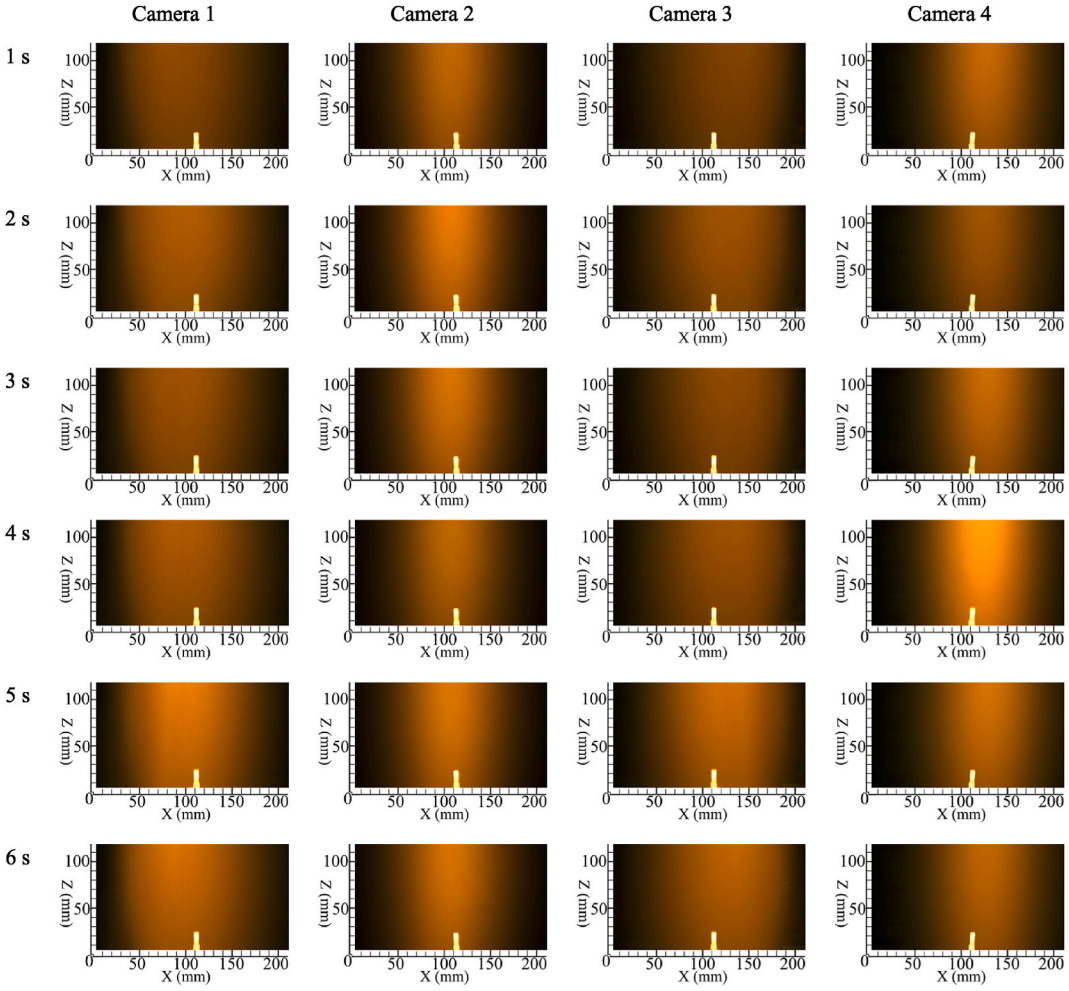

Fig. 8. Images of afterburner flame at different times.

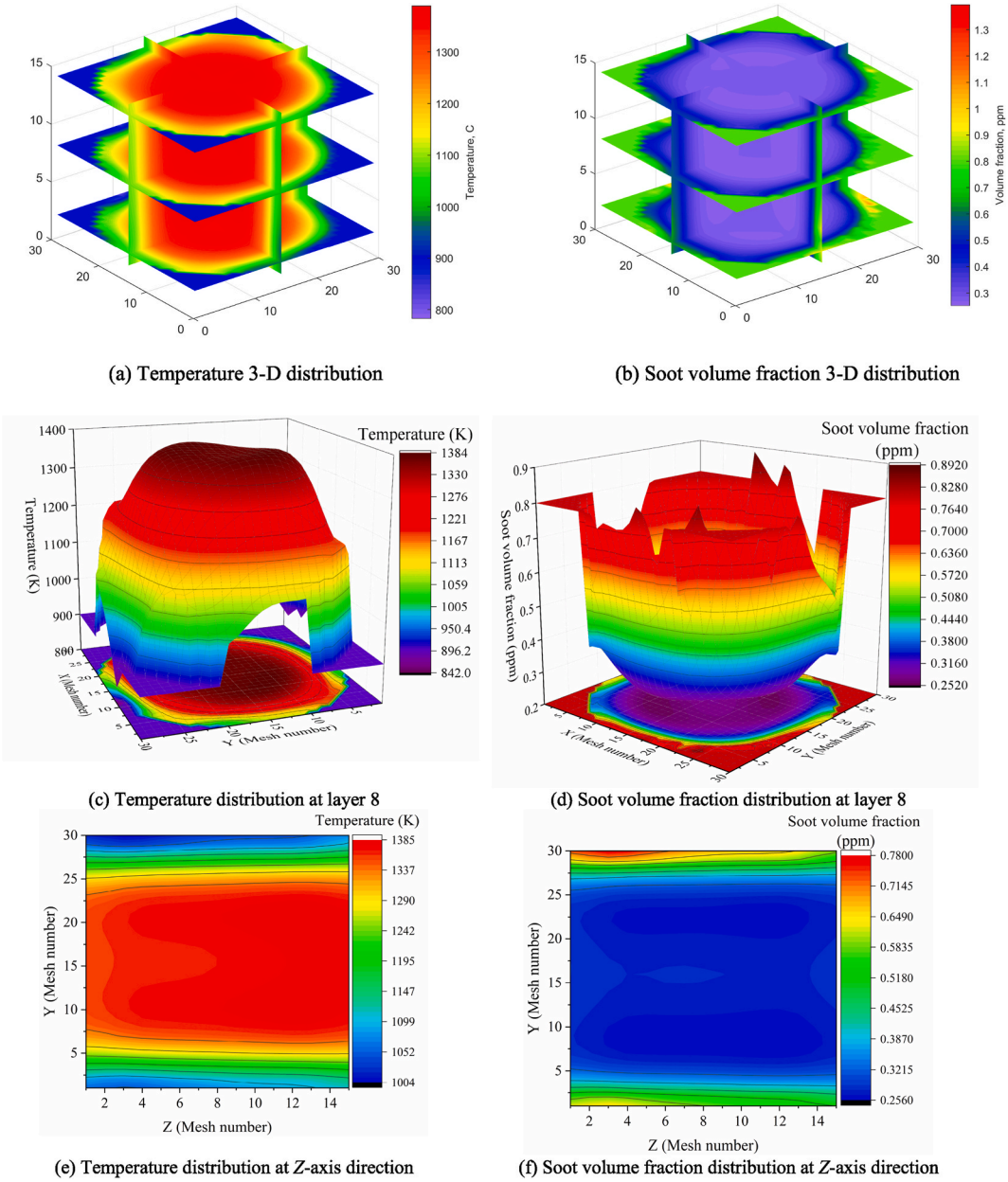

Fig. 9. The soot temperature and volume fraction 3-D reconstruction results of afterburner flame.

reconstruct the 3-D soot temperature and volume fraction.

Fig. 9 reveals the reconstructed afterburner flame in this experiment. (a) and (b) are the 3-D distribution of the soot temperature and volume fraction respectively. These figures demonstrate that the temperature peak appeared in the center of the reconstruction area; whereas the distribution of soot volume fraction was opposite to that. It can be seen from Fig. 9 (c) and (d) that the highest temperature was 1384 K and the minimum soot volume fraction was 0.252 ppm. Fig. 9 (e) and (f) illustrate the sliced soot temperature and volume fraction distribution across the *Y-Z* cross-sectional area on layer 15 of the *X*-axis. The temperature at (*Y* 15, *Z* 1) was 1349.61 K, and in the same location, the temperature captured by the thermometer was 1344.03 K.

Fig. 10 shows the comparison between thermocouple measured temperature and 3-D reconstructed temperature at different times. The measurements with the thermocouple and 3-D reconstruction had a similar rising and falling trend The maximum difference between the measured temperature by the thermocouple and 3-D reconstruction was 24 K, which occurs at the beginning of combustion, which was caused by the low signal-to-noise ratio of the cameras at the beginning of flame combustion. The two measured values became closer with the increase of afterburner flame temperature. During the 5–6 s, the temperature discrepancy of thermocouples and optical measurements is reduced, the main reason is that the thermocouple intrusion the flame, and the thermal inertia of

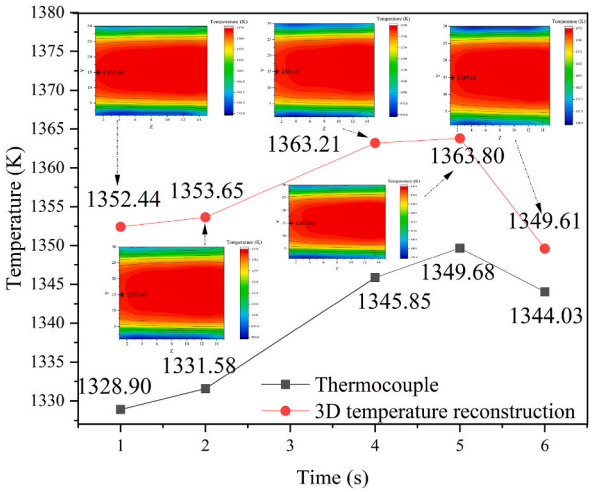

Fig. 10. The temperature comparison between the thermocouple and 3-D reconstruction.

the thermocouple leads to the measured temperature of the thermocouple being higher than the real temperature. The measured temperature by the thermocouple was slightly lower than that by 3-D reconstruction all the time.

4. Conclusions

In this paper, a novel method has been introduced, which was developed by combining stereo camera calibration and 3-D emission measurement techniques. The theoretical analysis and experimental results confirm that this method can achieve good measurement accuracy with a high 3-D spatial resolution for soot temperature and volume fraction reconstruction of afterburner flame, the following conclusions can be drawn:

(1) The relative measurement error rose with the increase of mesh density rapidly. In each layer of the *XY* plane along the *Z*-axis, the error peaked at the center of the given layer for both temperature and volume fraction reconstruction. Additionally, the peak relative error of all volume elements occurs around the body center of the reconstruction area.
(2) For the same mesh density, the relative error of volume fraction was larger than that of temperature. The average relative error under the condition with rotation correction only was significantly higher than that with translation correction only for both temperature and volume fraction reconstruction, which may be caused by the larger offset value of translation in this experiment, hence it was probably unique for the experiment conducted in this research.
(3) The sparser mesh density of 30*30*15 was adopted to reconstruct the afterburner flame in the experiments because the average relative error of soot temperature and volume fraction reached the lowest values of 3.17e-5% and 0.051%, respectively.
(4) The temperature measurement values provided with the thermocouple and with the 3-D reconstruction method at different times had the same trend. The maximum temperature measurement difference between these two methods was 24 K, which occurred at the beginning of combustion, and the difference reduced gradually with increasing afterburner flame temperature.

From this research, it can be confirmed that the proposed 3-D emission measurement technique developed in this research has its advantages in afterburner flame mapping, which offers high 3-D spatial resolution and good measurement accuracy.

Author statement

Minglu Dai: Ideas, Methodology, Software. **Bin Zhou:** Formal analysis, Resources, Supervision. **Jianyong Zhang:** Visualization, Investigation, Writing - Original Draft. **Bingxian Zuo:** Data Curation, Software. **Yihong Wang:** Writing- Reviewing and Editing.

Declaration of competing interest

The authors declare that they have no known competing financial interests or personal relationships that could have appeared to influence the work reported in this paper.

Acknowledgment

This work was supported by the National Natural Science Foundation of China, Project No.50906013 and No.50976024.

References

[1] C.K.W. Tam, S.A. Parrish, Noise of high-performance aircraft at afterburner, J. Sound Vib. 352 (2015) 103–128.

[2] J. Miao, Y. Fan, W. Wu, S. Zhao, Influence of air-entraining intensity on the afterburner ignition, flame-holding and combustion characteristics, Aero. Sci. Technol. 106 (2020).
[3] H.C. Bheemul, G. Lu, Y. Yan, Three-dimensional visualization and quantitative characterization of gaseous flames, Meas. Sci. Technol. 13 (2002) 1643.
[4] C. Lou, H. Zhou, Deduction of the two-dimensional distribution of temperature in a cross section of a boiler furnace from images of flame radiation, Combust. Flame 143 (2005) 97–105.
[5] H.-C. Zhou, C. Lou, Q. Cheng, Z. Jiang, J. He, B. Huang, Z. Pei, C. Lu, Experimental investigations on visualization of three-dimensional temperature distributions in a large-scale pulverized-coal-fired boiler furnace, Proc. Combust. Inst. 30 (2005) 1699–1706.
[6] Y.-t. Chu, C. Lou, Q. Cheng, H.-c. Zhou, Distributed parameter modeling and simulation for the evaporation system of a controlled circulation boiler based on 3-D combustion monitoring, Appl. Therm. Eng. 28 (2008) 164–177.
[7] D. Liu, Q.X. Huang, F. Wang, Y. Chi, K.F. Cen, J.H. Yan, Simultaneous measurement of three-dimensional soot temperature and volume fraction fields in axisymmetric or asymmetric small unconfined flames with CCD cameras, J. Heat Tran. (2010) 132.
[8] W. Yan, C. Lou, Two-dimensional distributions of temperature and soot volume fraction inversed from visible flame images, Exp. Therm. Fluid Sci. 50 (2013) 229–233.
[9] W. Yan, H. Zhou, Z. Jiang, C. Lou, X. Zhang, D. Chen, Experiments on measurement of temperature and emissivity of municipal solid waste (MSW) combustion by spectral analysis and image processing in visible spectrum, Energy Fuels 27 (2013) 6754–6762.
[10] W. Yan, D. Chen, Z. Yang, E. Yan, P. Zhao, Measurement of soot volume fraction and temperature for oxygen-enriched ethylene combustion based on flame image processing, Energies 10 (2017).
[11] Z. Xiangyu, L. Xu, Y. yu, Z. Bo, X. Hongjie, Temperature measurement of coal fired flame in the cement kiln by raw image processing, Measurement 129 (2018) 471–478.
[12] Y.-c. Zhang, B. Wei, X.-b. Fu, An unsteady temperature field measurement method for large hot cylindrical shell forging based on infrared spectrum, Measurement 58 (2014) 12–20.
[13] M. Ni, H. Zhang, F. Wang, Z. Xie, Q. Huang, J. Yan, K. Cen, Study on the detection of three-dimensional soot temperature and volume fraction fields of a laminar flame by multispectral imaging system, Appl. Therm. Eng. 96 (2016) 421–431.
[14] M. Li, K. Sun, Z. He, Integrated research of a multi-wavelength method in anisotropic scattering flame on soot temperature and radiative coefficient reconstruction, Appl. Opt. 57 (2018) 5899–5913.
[15] Y. Xu, Y. Zhao, F. Wu, K. Yang, Error analysis of calibration parameters estimation for binocular stereo vision system, in: 2013 IEEE International Conference on Imaging Systems and Techniques (IST), IEEE, 2013, pp. 317–320.
[16] O. Kahmen, R. Rofallski, T. Luhmann, Impact of stereo camera calibration to object accuracy in multimedia photogrammetry, Rem. Sens. 12 (2020).
[17] R. Usamentiaga, D.F. Garcia, Multi-camera calibration for accurate geometric measurements in industrial environments, Measurement 134 (2019) 345–358.
[18] Y. Furukawa, J. Ponce, Accurate camera calibration from multi-view stereo and bundle adjustment, Int. J. Comput. Vis. 84 (2009) 257–268.
[19] K. Genovese, Y. Chi, B. Pan, Stereo-camera calibration for large-scale DIC measurements with active phase targets and planar mirrors, Opt Express 27 (2019) 9040–9053.
[20] M.F. Modest, Radiative Heat Transfer, Academic press, 2013.
[21] W. Cai, C.F. Kaminski, Tomographic absorption spectroscopy for the study of gas dynamics and reactive flows, Prog. Energy Combust. Sci. 59 (2017) 1–31.
[22] K. Daun, Infrared species limited data tomography through Tikhonov reconstruction, J. Quant. Spectrosc. Radiat. Transf. 111 (2010) 105–115.
[23] C. Wei, K.K. Schwarm, D.I. Pineda, R.M. Spearrin, Volumetric laser absorption imaging of temperature, CO and CO2 in laminar flames using 3D masked Tikhonov regularization, Combust. Flame 224 (2021) 239–247.
[24] O.D. Montoya, Numerical approximation of the maximum power consumption in DC-MGs with CPLs via an SDP model, IEEE Trans. Circuits Syst. II: Express Briefs 66 (2018) 642–646.
[25] R. Gu, M. Sun, Z. Cai, P. Li, Y. Huang, Numerical modeling and experimental investigation on the rocket-ejector system with limited mixer length, Acta Astronaut. 182 (2021) 13–20.
[26] T. Parameswaran, R. Hughes, P. Gogolek, P. Hughes, Gasification temperature measurement with flame emission spectroscopy, Fuel 134 (2014) 579–587.
[27] Y. Sun, C. Lou, H. Zhou, A simple judgment method of gray property of flames based on spectral analysis and the two-color method for measurements of temperatures and emissivity, Proc. Combust. Inst. 33 (2011) 735–741.
[28] S. Zheng, Y. Yang, X. Li, H. Liu, W. Yan, R. Sui, Q. Lu, Temperature and emissivity measurements from combustion of pine wood, rice husk and fir wood using flame emission spectrum, Fuel Process. Technol. 204 (2020) 106423.